American Mineralogist, Volume 103, pages 241–251, 2018

Conversion of serpentine to smectite under hydrothermal condition: Implication for solid-state transformation

Shichao Ji[1,2], Jianxi Zhu[1], Hongping He[1,2]*, Qi Tao[1], Runliang Zhu[1], Lingya Ma[1], Meng Chen[1], Shangying Li[1,2], and Junming Zhou[1,2]

[1]Key Laboratory of Mineralogy and Metallogeny, Chinese Academy of Sciences & Guangdong Provincial Key Laboratory of Mineral Physics and Materials, Guangzhou Institute of Geochemistry, Guangzhou 510640, China
[2]University of Chinese Academy of Sciences, Beijing 100049, China

Abstract

Understanding clay mineral transformation is of fundamental importance to grasping phyllosilicate crystal chemistry and unraveling geochemical processes. In this study, hydrothermal experiments were conducted on lizardite and antigorite, to investigate the possibility of the transformation from serpentine to smectite, the effect of precursor minerals' structure on the transformation and the transformation mechanism involved. The reaction products were characterized using XRD, TG, HRTEM, and ^{27}Al MAS NMR. The results show that both lizardite and antigorite can be converted to smectite, but such conversion is much more difficult than that of kaolinite group minerals. The successful transformation is mainly evidenced by the occurrence of the characteristic (001) reflection of smectite at 1.2–1.3 nm in the XRD patterns and smectite layers with a thickness of 1.2–1.3 nm in HRTEM images of hydrothermal products as well as the dehydroxylation of the newly formed smectite at a higher temperature in comparison to that of the starting minerals. The difficulty for the transformation of serpentine to smectite may be due to the lack of enough available Al in the reaction system, in which the substitution of Al^{3+} for Si^{4+} in the neo-formed tetrahedral sheet is critical to control the size matching between the neo-formed tetrahedral sheet and octahedral sheet in starting minerals. Since the neighboring layers in antigorite are linked by the strong Si-O covalent bonds, the transformation only takes place at the edges of an antigorite layer rather than the whole layer, and the neo-formed smectite is non-swelling due to the inheritance of such Si-O covalent bonds. The conversion of lizardite to smectite is more feasible than that of antigorite, accompanied by exfoliation. This leads to a prominent decrease of the particle size in the hydrothermal products and the number of phyllosilicate layers contained therein. Two dominant pathways were observed for the transformation of lizardite and antigorite into smectite, i.e., conversion of one serpentine layer to one smectite layer via attachment of Si-O tetrahedra onto the octahedral sheet surface of the starting minerals and two adjacent serpentine layers merging into one smectite layer. In the case of the latter, dissolution of octahedra and inversion of tetrahedral sheets took place during the transformation. Besides these two dominant pathways, precipitation and epitaxial growth of smectite were also observed in the cases of lizardite and antigorite, respectively. The present study suggests that solid-state transformation is the main mechanism for conversion of serpentine minerals to smectite, similar to the transformation of kaolinite group minerals to beidellite.

Keywords: Clay transformation, solid-state transformation, hydrothermal condition, serpentine mineral, smectite

Introduction

Clay minerals are ubiquitous on the Earth's surface that can be transformed into other phyllosilicates in various geological and geochemical processes (e.g., weathering, diagenesis, and metamorphism) (Wildman et al. 1968; Dunoyer de Segonzac 1970; Hower et al. 1976; Lanson et al. 1996; Stripp et al. 2006). Transformation mechanisms and resulting products are controlled by geochemical environments in which a transformation takes place. Accordingly, chemical changes and mineralogical transformations can provide important constrains for the geochemical conditions that cause these processes. And, in turn, these transformations can exert influences on the cycling of elements in the related environments, due to the high surface-to-volume ratio and surface reactivity of clay minerals (Cuadros 2012).

So far, mostly reported are the transformations among 2:1 type clay minerals (e.g., illitization of smectite, glauconitization of smectite) (Weaver 1958; Boles and Franks 1979; Odin 1988; Lindgreen et al. 2000) and from 2:1 type to 1:1 type (e.g., kaolinization of smectite) (Altschuler et al. 1963; Righi et al. 1999; Ryan and Huertas 2013). Chloritization of 1:1 type clay minerals (e.g., serpentine, berthierine) (Banfield and Bailey 1996; Xu and Veblen 1996; Ryan and Reynolds 1997), a conver-

* E-mail: hehp@gig.ac.cn

0003-004X/18/0002–241$05.00/DOI: https://doi.org/10.2138/am-2018-6183CCBYNCND

sion of 1:1 type to 2:1 type, mainly takes place in the subsurface of geological systems (Beaufort et al. 2015). Based on the investigations of natural and synthetic samples, two mechanisms have been proposed for clay transformations: (1) conversion in solid state by atom rearrangement with the interlayer as the main route for atom diffusion in and out of the structure; (2) dissolution of the original mineral and recrystallization of the new structure phase (Pollard 1971; Nadeau et al. 1985; Dudek et al. 2006; He et al. 2017). The reported studies suggest that the solid-state transformation mechanism prevails in weathering environments (Mackumbi and Herbillon 1972; Banfield and Murakami 1998; Wilson 2004), while in diagenetic and hydrothermal environments, the occurrence of either solid-state or dissolution-recrystallization transformation appears to be largely controlled by fluid-to-rock ratio (Altaner and Ylagan 1997).

In comparison to the transformation pathways among 2:1 type clay minerals and from 2:1 type to 1:1 type, the conversion of 1:1 type clay minerals to 2:1 type ones is less commonly observed on the Earth's surface. As reported in literature (Coombe et al. 1956; Ducloux et al. 1976; Istok and Harward 1982; Graham et al. 1990; Bonifacio et al. 1997; Lee et al. 2003), 2:1 type clay minerals are mainly formed in the procedures of weathering and pedogenesis, in which 1:1 type clay minerals were dissolved and provided the elemental sources for recrystallization of 2:1 type ones, i.e., a dissolution-recrystallization mechanism is involved in the transformations. Recently, our hydrothermal experiments show that both kaolinite and halloysite (i.e., 1:1 type clay minerals) can be converted to beidelite (i.e., 2:1 type clay minerals) via a solid-state mechanism (He et al. 2017). In this procedure, attachment of a newly formed Si-O tetrahedral sheet to the 1:1 layer of precursor mineral is a critical step for successful transformation. Simultaneously, the substitution of Al^{3+} for Si^{4+} in the neo-formed tetrahedral sheets can greatly improve the size matching between the octahedral sheet of the precursor mineral and the neo-formed tetrahedral sheet. However, a few new insights and further clarifications are needed, including: (1) whether other 1:1 type clay minerals (e.g., serpentine), besides kaolinite and halloysite, can be converted to smectite under hydrothermal condition? (2) What is the effect of the precursor phase structure on the transformation? (3) Whether isomorphous substitutions in the neo-formed tetrahedral sheets (e.g., Al^{3+} for Si^{4+}) is essential for the conversion of serpentine to 2:1 type clay minerals? (The Al content in serpentine minerals is much lower than that in kaolinite group minerals.) Hence, this paper, as a companion study of our recent work on the transformation of kaolinite and halloysite to beidellite (He et al. 2017), reports our latest investigations on the transformation of serpentines (e.g., lizardite and antigorite) into smectite under identical hydrothermal condition.

Materials and methods

Starting materials

Two kinds of serpentine minerals with different structures, lizardite and antigorite, were used in the transformation experiments. The lizardite sample (L) was collected from Taitung County, Taiwan Province, China, and the geological details were summarized by Chang et al. (2000). The antigorite sample (A) was collected from the serpentinized dolomitic marble, which belongs to Proterozoic carbonate strata (Xiuyan County, Liaoning Province, China). Their chemical compositions are presented in Table 1, determined by using X-ray fluorescence spectroscopy (XRF) (He et al. 2014).

Lizardite has a flat crystal structure with the correct geometry of interlayer H-bonds, which is favored by the coupled substitution of Al^{3+} or Fe^{3+} for Mg^{2+} in octahedral sheets and Si^{4+} in tetrahedral sheets (Evans et al. 2013). Antigorite displays curved, wavy layers similar to Roman tiles on a roof. The octahedral sheet is continuous and wavy, whereas the tetrahedral sheet undergoes periodic reversals along the *a* axis so that it connects to the concave half-waves of adjacent octahedral sheets (Otten 1993; Grobéty 2003; Capitani and Mellini 2004; Evans et al. 2013). The reversals allow serpentine layers to be bound through strong covalent Si–O bonds (Evans et al. 2013). The large superstructure of antigorite along the [100] direction is a result of this repeating wave structure (Zussman 1954; Kunze 1956, 1958, 1961; Uehara 1988). In this study, the supercell repeat-unit in antigorite is approximately 3.1 nm, which is determined by the selected-area electron diffraction (SAED) patterns (see HRTEM observation and EDS analysis) (Whittaker and Zussman 1956; Zussman et al. 1957; Kunze 1961; Uehara and Shirozu 1985; Uehara 1988; Palacios-Lidon et al. 2010).

Sodium metasilicate ($Na_2SiO_3 \cdot 9H_2O$) of analytical grade was used as the Si source for the transformation experiments.

Experimental methods

The hydrothermal experiments were conducted in a stainless steel autoclave at 300 °C under an autogenous water pressure. The Mg/Si ratios in the starting mixture of sodium metasilicate and serpentine were fixed at 3:4, close to that of saponite. The experiment procedure was as follows: 24 g of sodium metasilicate was dissolved into 100 mL deionized water with continuous stirring. The pH of the solution was adjusted to 8 by hydrochloric acid under vigorous stirring. Then, the obtained sol-gel was transferred into a stainless steel autoclave and mixed with 3.5 g of serpentine. The mixture was hydrothermally treated in the autoclave at 300 °C under an autogenous water pressure for one to two weeks. The obtained products were washed 6 times using deionized water to remove electrolytes, and then dried at 80 °C for 24 h and ground before characterization. The products were marked as X-xw, in which X = L or A, standing for lizardite or antigorite, respectively, and xw stands for the duration of the treatment time, i.e., 1w = 1 week and 2w = 2 weeks. The experimental conditions adopted in this study are summarized in Table 2.

Characterization techniques

X-ray diffraction (XRD). XRD patterns were collected on a Bruker D8 Advance diffractometer with Ni-filtered Cu*K*α radiation (λ = 0.154 nm, 40 kV and 40 mA) at a scanning rate of 1° (2θ) min^{-1} between 3 and 30° (2θ). The powder XRD patterns were used for the determination of mineral contents in the hydrothermal products, where pure Si was selected as the internal standard. The

Table 1. Chemical composition of lizardite and antigorite

	Al_2O_3	CaO	Fe_2O_3	K_2O	MgO	Na_2O	SiO_2	TiO_2	H_2O	Total (%)
Lizardite	0.59	0.02	7.78	–	37.5	0.13	38.95	–	14.19	99.16
Antigorite	0.09	0.04	0.60	–	42.0	0.13	44.67	–	12.33	99.86

Table 2. Experimental conditions and basal spacings (nm) of serpentine and neo-formed smectite

t (w)[a]	Sample	*T* (°C)	*P* (MPa)[b]	XRD[c] Powdered	XRD[c] Glycolated	TEM[d]	%S[e]
			Starting minerals				
0	L	–	–	0.72	0.72	0.72	0
0	A	–	–	0.72	0.72	0.72	0
			Products from lizardite				
1	L-1w	300	~8.6	1.27	1.70	1.24–1.30	~43.7
2	L-2w	300	~8.6	1.27	1.71	1.20–1.31	~57.3
			Products from antigorite				
1	A-1w	300	~8.6	1.26	1.25	1.22–1.26	~27.4
2	A-2w	300	~8.6	1.24	1.24	1.23–1.25	~28.3

[a] t stands for the duration of the treatment time and w is short for week, i.e., 1w = 1 week and 2w = 2 weeks.
[b] *P* is the autogenous water pressure at 300 °C.
[c] Only the basal spacings of neo-formed smectite are listed for the hydrothermal products.
[d] The values are determined based on selected area electron diffractions.
[e] The ratio of the newly formed smectite (S) in the hydrothermal products, determined by the powder XRD patterns.

methods for sample preparation and the mineral content analysis were described by Brindley (1980b). The oriented samples were prepared by adding 15 mg solid products into 1 mL deionized water, followed by ultrasonic dispersion for 2 min. Then, the suspension was added onto a glass slide dropwise and dried at ambient temperature. Glycolated samples were prepared by treating the oriented samples in a glass desiccator with ethylene glycol at ambient temperature for 24 h.

Thermogravimetric analysis (TG). TG analyses were performed on a Netzsch STA 409PC instrument. Approximately 15 mg ground sample was heated in a corundum crucible from 30 to 1000 °C at a heating rate of 10 °C/min under a pure N_2 atmosphere (60 cm^3/min). The differential thermogravimetric (DTG) curve was derived from the TG curve.

High-resolution transmission electron microscopy (HRTEM). To investigate the silicate layers of entire crystals or particles in the direction parallel to the *c* axis, sample are oriented embedded in epoxy resin. Then, ultrathin sections (~75 nm) were ultramicrotomed with a diamond knife using a Lecia EM UC7 and mounted on holey carbon-coated TEM copper grids. HRTEM images, X-ray energy-dispersive spectroscopy (EDS), and selected-area electron diffraction (SAED) analyses were carried out using a FEI Talos F200S high-resolution transmission electron microscope equipped with Super-X X-ray spectroscopy, and operated at 200 kV.

Magic-angle-spinning nuclear magnetic resonance spectroscopy (MAS NMR). ^{27}Al MAS NMR spectra were obtained on Bruker AVANCE III 600 spectrometer at resonance frequency of 156.4 MHz. A 4 mm HX double-resonance MAS probe was used to measure ^{27}Al MAS NMR at a sample spinning rate of 14 kHz. The spectra were recorded by a small-flip angle technique with a pulse length of 0.5 μs (<π/12) and a 1 s recycle delay. The chemical shift of ^{27}Al was referenced to 1 M aqueous $Al(NO_3)_3$.

RESULTS

XRD patterns

XRD patterns of both lizardite and antigorite display characteristic basal spacings at 0.72 nm (Mellini 1982; Uehara and Shirozu 1985) without any reflections from impurity minerals (Fig. 1), indicating that the starting minerals are of high purity. In the case of lizardite, the intensity of (001) reflection dramatically decreases after hydrothermal treatment, which is accompanied by the occurrence of three new reflections at 0.33, 0.42, and 1.27 nm, respectively (Fig. 1a). The intense reflections at 0.33 and 0.42 nm correspond well to (101) and (100) planes of quartz, which are formed by the polymerization of metasilicate (Wooster and Wooster 1946). Upon ethylene glycolation, the reflection at approximately 1.27 nm shifts to 1.70 nm, displaying a swelling property of the corresponding mineral. This suggests the newly formed mineral should be smectite (Mosser-Ruck et al. 2005; He et al. 2017). As one of the starting materials is $Na_2SiO_3 \cdot 9H_2O$, the resultant smectite may have Na^+ as its interlayer cation, consistent with the d_{001} of 1.27 nm (Suquet et al. 1975; Ferrage et al. 2010).

It is noteworthy that the characteristic reflections of the neo-formed smectite is very weak and broad, implying poor crystallinity as well as low layer-stacking order (He et al. 2014). Meanwhile, as indicated by XRD patterns (Fig. 1), the reflection intensity of quartz increases with the extension of hydrothermal reaction duration from one week (L-1w) to two weeks (L-2w). Since the stoichiometric ratios of Mg/Si in the starting materials are 3:4, close to that of saponite, the formation of quartz suggests that only part of the added metasilicate involves in the transformation and the conversion of lizardite to smectite (i.e., saponite in this study) is more difficult than halloysite and kaolinite (He et al. 2017).

The transformation of antigorite seems to be different from that of lizardite, indicated by XRD patterns (Figs. 1d–1f). After hydrothermal treatment, the reflections of antigorite are still prominent with a slight decrease of the reflection intensity [e.g., the (001) reflection at 0.72 nm]. Simultaneously, the characteristic reflections of newly formed quartz and smectite are observed at 0.33 and 1.24 nm, respectively (Fig. 1d). It is noteworthy that an intense (001) reflection of neo-formed smectite at 1.24 nm was recorded in the oriented XRD pattern of the two weeks' hydrothermal product (A-2w-O). More importantly, this basal spacing does not have any change upon ethylene glycolation (Fig. 1f), implying that the microstructure of hydrothermal products is different from the ones transformed from lizardite in this study and those from kaolinite group minerals (Ryu et al. 2006; He et al. 2017).

Thermal analysis

The TG and DTG curves of samples are presented in Figure 2. A prominent mass loss of lizardite, corresponding to dehydroxylation, occurs at approximately 608 °C, while the mass loss of adsorbed water was recorded at around 100 °C (Fig. 2a). The dehydroxylation temperature of lizardite in this study is obviously lower than that of serpentine minerals (i.e., lizardite, antigorite, and chrysotile) reported by Viti (2010). After hydrothermal treatment, the mass loss of dehydroxylation dramatically decreases and a new mass loss occurs at approximately 750 °C (Figs. 2b and 2c). The significant decrease of the dehydroxylation mass loss is attributed to the consumption of inner-surface hydroxyls in starting minerals during the transformation of 1:1 type clay minerals into 2:1 type ones (He et al. 2017). Theoretically, about two-thirds of inner-surface hydroxyls in 1:1 type precursor minerals will be consumed during the transformation, through the

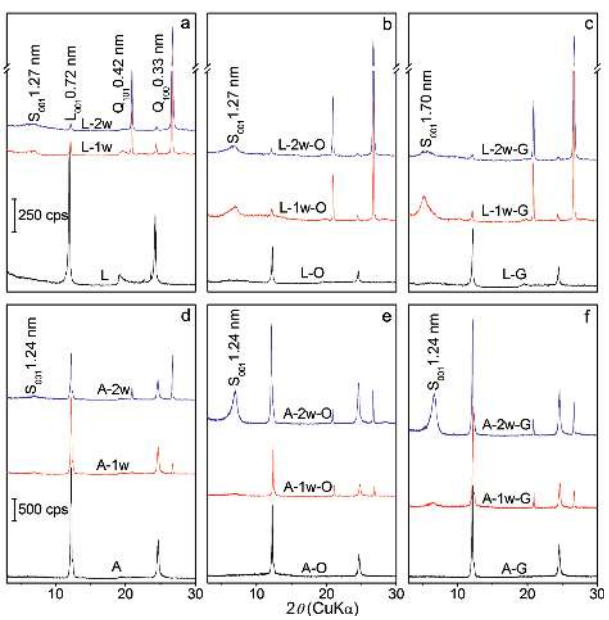

FIGURE 1. XRD patterns of lizardite, antigorite, and their hydrothermal products with sodium metasilicate. (**a**) Randomly oriented lizardite (L) and its hydrothermal products (L-1w and L-2w). (**b**) Oriented lizardite and its hydrothermal products (L-1w-O and L-2w-O). (**c**) Glycolated lizardite and its hydrothermal products (L-1w-G and L-2w-G). (**d–f**) Randomly oriented, oriented, and glycolated samples of antigorite and its hydrothermal products. (S = smectite, L = lizardite, Q = quartz, O = oriented sample, G = glycolated sample.)

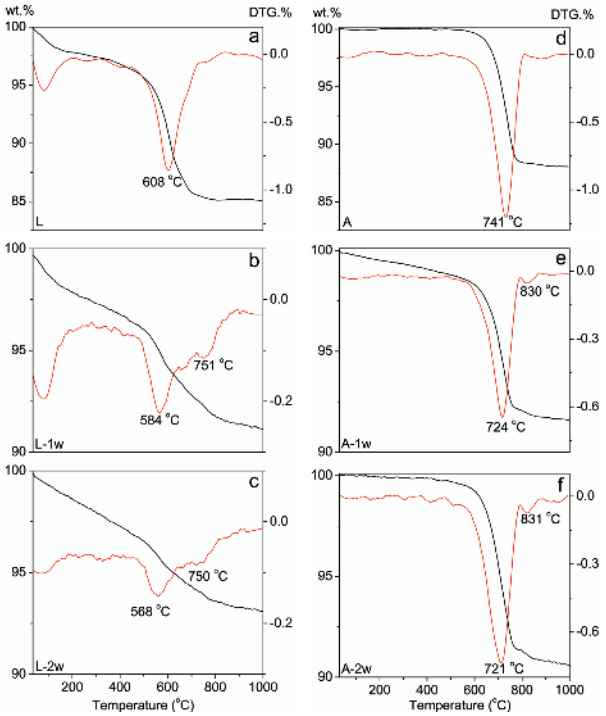

Figure 2. Thermal analyses of serpentine and their hydrothermal products in N_2 atmosphere (wt%, TG and %, DTG). (**a**) Lizardite and (**b** and **c**) its hydrothermal products treated with sodium metasilicate, (**d**) antigorite and (**e** and **f**) its hydrothermal products treated with sodium metasilicate.

condensation between inner-surface hydroxyls and hydrolyzed metasilicate (He et al. 2017).

The TG and DTG curves of antigorite and its hydrothermal products display prominent differences in comparison to those of lizardite and its hydrothermal products (Figs. 2d–2f). The TG curve of antigorite only shows one main mass loss around 740 °C, corresponding to dehydroxylation, and no obvious mass loss of adsorbed water was observed at approximately 100 °C (Fig. 2e). Dehydroxylation temperature of antigorite is different from those reported in literature (Viti 2010), in which the main mass loss of dehydroxylation occurs at 713–720 °C, coupled with a mass loss at higher temperature (e.g., 743–760 °C) and a shoulder at lower temperature (e.g., 636–645 °C). For the hydrothermally treated products, the starting and end temperatures of the dominant mass loss, corresponding to the dehydroxylation of antigorite, are almost identical to those of the precursor mineral while the center of corresponding DTG peak shifts to 720 °C (Figs. 2e and 2f). Simultaneously, a minor mass loss occurs at approximately 830 °C (Figs. 2e and 2f), attributed to the dehydroxylation of the newly formed smectite. The thermal analysis results suggest that most of the antigorite precursor remains unchanged with a minor part converted to smectite, in agreement with the XRD results (Fig. 1d).

HRTEM observation and EDS analysis

HRTEM images of both lizardite and antigorite before and after hydrothermal treatments clearly display prominent morphological changes and structural evolution of clay mineral layers (Figs. 3–6). Generally, both newly formed smectite

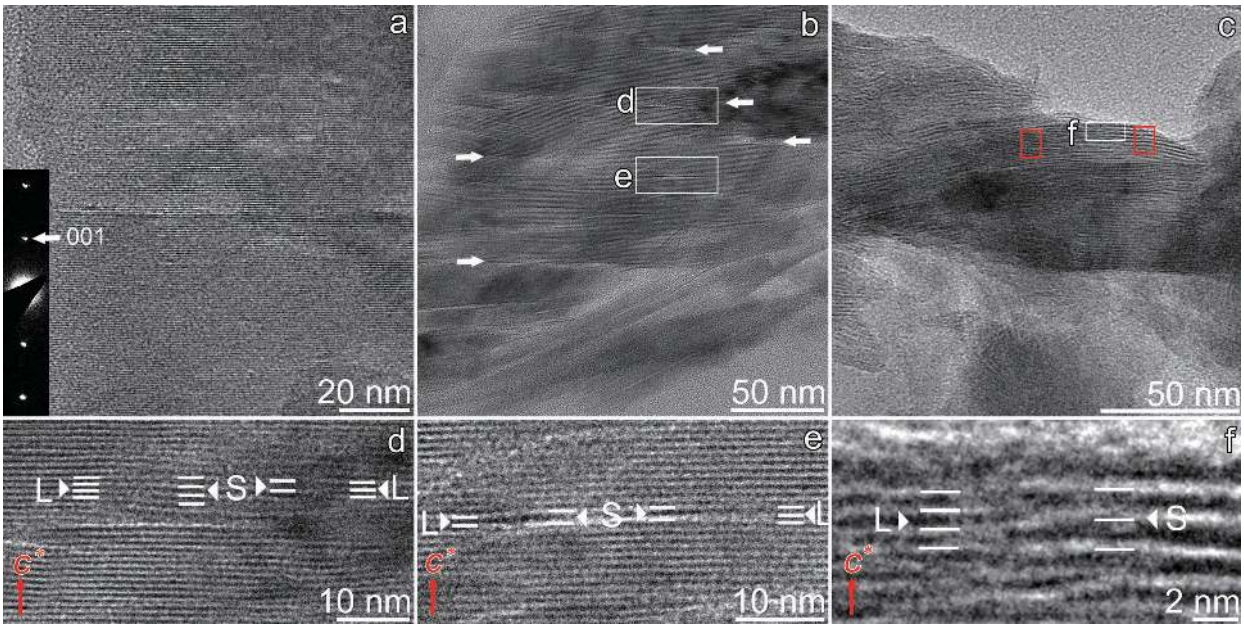

Figure 3. HRTEM images of (**a**) lizardite, and (**b–f**) its hydrothermal products with sodium metasilicate. Smectite layers with a thickness of approximately 1.3 nm was observed in the hydrothermal products. (**b**) Hydrothermal products after treatment for one week (L-1w). Layer distortion occurs within lizardite domains. (**c**) Hydrothermal products after treatment for two weeks (L-2w). Fifteen lizardite layers are observed in the red rectangle at the central part of the particle, while there are only eight smectite layers in the red rectangle at the edge. (**d** and **e**) Enlarged areas of the outlined areas (the white rectangles) in **b**. The lizardite layers are directly transformed into smectite layers at the left part, while two lizardite layers merge into one smectite layer at the right part. (**f**) Higher magnification of the selected area (the white square) in **e**. (L = lizardite, S = smectite).

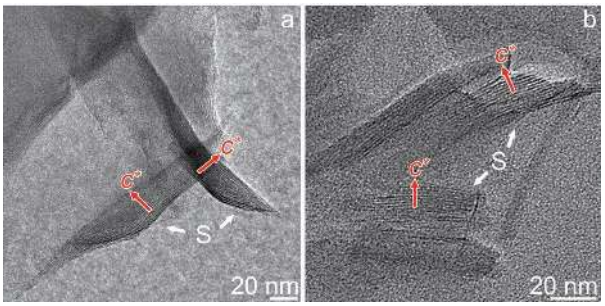

Figure 4. HRTEM images of the hydrothermal products from lizardite. (**a** and **b**) Pure smectite particles with a layer thickness of approximately 1.3 nm, without any lizardite layers.

layers with a thickness of 1.2–1.3 nm (Schumann et al. 2013) and the serpentine layers of the starting minerals with a thickness of approximately 0.7 nm are observed in all hydrothermal products. X-ray EDS analyses reveal that the Si/Mg ratios of the newly formed smectite layers are almost identical with the reported values in smectite (Fig. 7) (Bergaya and Lagaly 2013). These results demonstrate that both lizardite and antigorite can be successfully transformed into smectite, consistent with the XRD results.

In the case of lizardite, smectite layers occur not only at the edge of the lizardite layers, but also within lizardite domains after hydrothermal treatment (Fig. 3). The starting mineral displays regular stacking layers with a thickness of 0.7 nm (Fig. 3a). However, after hydrothermal treatment, distorted phyllosilicate layers are extensively observed within lizardite domains, where the transformation of lizardite into smectite takes place (indicated by the white arrows in Fig. 3b). The layer-stacking order of lizardite was destroyed by these distortions, and large lizardite particles were split into several smaller ones. Meanwhile, the particle size in Sample L-2w (Fig. 3c) is smaller than that in Sample L-1w (Fig. 3b), implying that the particle size and the number of phyllosilicate layers contained therein deceases with an extension of hydrothermal treatment time. This may lead to the weak (001) reflections of the hydrothermal products from lizardite (Figs. 1a–1c) (Brindley 1980a).

Two different pathways are observed in the transformation of lizardite into smectite. As shown by the HRTEM images of L-1w (Figs. 3d and 3e, enlarged areas of the outlined areas in Fig. 3b), the lizardite layers were directly converted to the same number of smectite layers at the left part, while two smectite layers were formed from three lizardite layers at the right part. More interestingly, the HRTEM images (the right part in Figs. 3d and 3e) clearly show that one of the three lizardite layers was converted to one smectite layer while the other two lizardite layers merged into one smectite layer. Similar transformation pathways are also observed in Sample L-2w, in which four lizardite layers were transformed into three smectite layers (Fig. 3f, enlarged area of the outlined area in Fig. 3c). These observations suggest that the smectite layers can be formed through different pathways from lizardite layers. Besides the dominant particles with coexistence of lizardite and smectite layers, a small amount of pure smectite particles without any lizardite layers are also observed in the hydrothermal products (Fig. 4). Most of these particles consist of only 3–20 smectite layers, and the size is significantly smaller than that of the particles with a coexistence of lizardite and smectite layers.

For the hydrothermal products from antigorite, neo-formed smectite layers only occur at the edges of antigorite particles (i.e., the neo-formed smectite layers are only formed at the edges of antigorite layers) (Figs. 5 and 6). Simultaneously, no significant decrease of particle size and distortion of antigorite layers is observed. These morphological characteristics are very different from the products from lizardite and can well explain the intense (001) reflection of antigorite in the hydrothermal products (Figs. 1d–1f). The length of the newly formed smectite layers at the edges of antigorite particles is approximately 5 nm in Sample A-1w, with poor crystallinity as well as low layer-stacking order (Fig. 5b), resulting in the weak basal reflections of smectite in the XRD patterns (Figs. 1d and 1e). With an extension of hydrothermal treatment time, the length of the smectite layers becomes slightly longer (5–10 nm) and the layer-stacking order

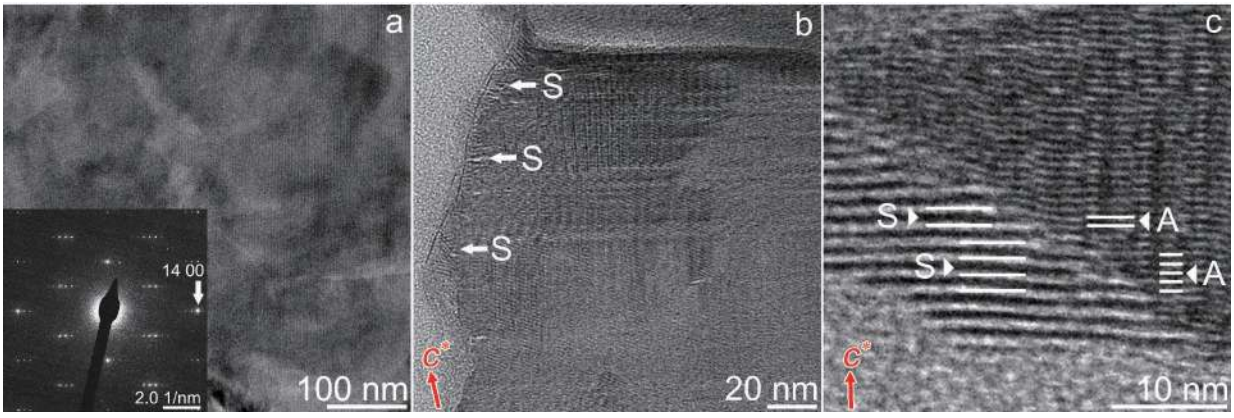

Figure 5. HRTEM images of (**a**) antigorite and (**b** and **c**) its hydrothermal products after treatment with sodium metasilicate. (**a**) SAED pattern of antigorite in *hk*0. The supercell repeat-unit in antigorite is approximately 3.1 nm, determined by SAED pattern. (**b** and **c**) Smectite layers with a thickness of approximately 1.3 nm occur only at the edge of the antigorite particles, and no layer distortion is observed. Two antigorite layers merge into one smectite layer. (A = antigorite, S = smectite.)

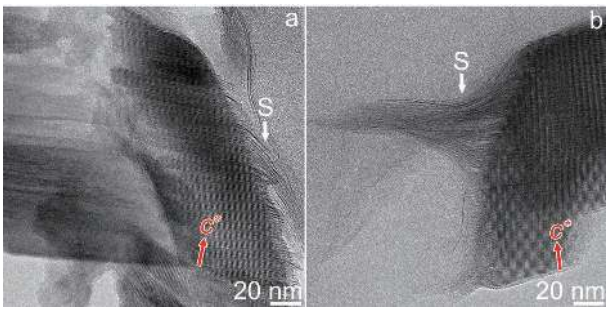

FIGURE 6. HRTEM images of hydrothermal products from antigorite after treatment with sodium metasilicate for two weeks. (S = smectite).

is increased. A small amount of smectite layers with several tens of nanometers in length can also be observed (Fig. 6). Since one end of the newly formed smectite layers, connecting with antigorite layers, is linked by the strong covalent Si–O bonds and they are very short in length as shown by HRTEM images (Figs. 5–6), the resulting smectite may not show swelling property. This is evidenced by the XRD measurements in which the basal reflection of smectite did not shift to 1.70 nm upon ethylene glycolation (Fig. 1f). Due to the very low Al content in the starting antigorite (Table 1), the newly formed smectite might be of low charge density.

Similar to the case of lizardite, both the merging of two antigorite layers into one smectite layer and the conversion of one antigorite layer to one smectite layer are observed. The former will lead to the number of neo-formed smectite layers obviously less than that of the neighboring antigorite layers (Fig. 5c). It is noteworthy that the length of a half supercell repeat-unit in antigorite is approximately 1.6 nm (i.e., the length of a supercell periodicity is ~3.1 nm), which is shorter than the length of the neo-formed smectite layers. This implies that the epitaxial growth of smectite layers might be also involved in the transformation procedure. These observations suggest that the structural difference between lizardite and antigorite has significant effects on the transformation and the mechanism involved.

EDS analyses supply supporting evidences for the successful transformation of lizardite and antigorite into smectite. The Si/Mg ratios of the neo-formed smectite layers are located in the range of 1.1–1.4 (Fig. 7), which is almost identical with the values of reported smectite. The Al/Mg ratios of the newly formed smectite are slightly higher than that of the corresponding lizardite and antigorite. This implies that the substitution of Al^{3+} for Si^{4+} may occur in the transformation of serpentine minerals into smectite, which is identified by ^{27}Al MAS NMR spectra.

^{27}Al MAS NMR spectra

^{27}Al MAS NMR spectrum of lizardite (Fig. 8a) displays a very weak and broad signal centered at 7.7 ppm, corresponding to sixfold-coordinated Al [Al(VI)] in octahedral sheets (Woessner 1989; Bentabol et al. 2010). In ^{27}Al MAS NMR spectra of hydrothermal products from lizardite, the signal at 7.7 ppm almost disappears and a new signal occurs at approximately 68 ppm (Fig. 8a), corresponding to the fourfold-coordinated Al [Al(IV)] in the Si-O tetrahedral sheets via the substitution of Al^{3+} for Si^{4+} (Woessner 1989; Bentabol et al. 2010). This implies the migration of Al^{3+} from octahedral sheets to tetrahedral ones during the transformation under hydrothermal condition (He et al. 2017).

The ^{27}Al MAS NMR spectrum of antigorite contains two signals at approximately 10 and 69 ppm (Fig. 8b), attributed to Al(VI) in octahedral sheets and Al(IV) in tetrahedral ones, respectively. After hydrothermal treatment, the Al(VI) signal at ca. 10 ppm decreases while that of Al(IV) signal obviously increases. Simultaneously, a new signal appears at approximately 60 ppm (Fig. 8b), which is assigned to Al in the three-dimensional silica framework (Breen et al. 1995). The intensity of this signal obviously increases with an extension of hydrothermal treatment time (Fig. 8b). As indicated by XRD patterns (Fig. 1), quartz formed during the transformation due to the polymerization of metasilicate. Thus, the signal at approximately 60 ppm should be attributed to the incorporation of Al into the newly formed quartz (He et al. 2017). These Al atoms are released into the solution due to the dissolution of octahedral sheets in serpentine minerals during the transformation.

DISCUSSION

Transformation from serpentine to smectite

Smectites are 2:1 type clay minerals with isomorphic substitutions in tetrahedral and/or octahedral sheets. The substitutions between cations with different valences result in the permanent

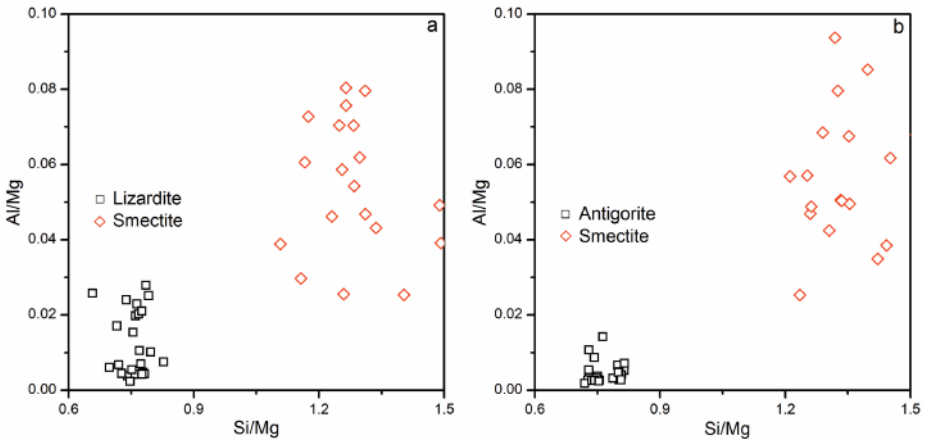

FIGURE 7. EDS analysis results of smectite and serpentine in the hydrothermal products. (**a**) The data are collected from the hydrothermal products of lizardite. (**b**) The data are collected from the hydrothermal products of antigorite. Square and diamond represent the serpentine and the newly formed smectite, respectively.

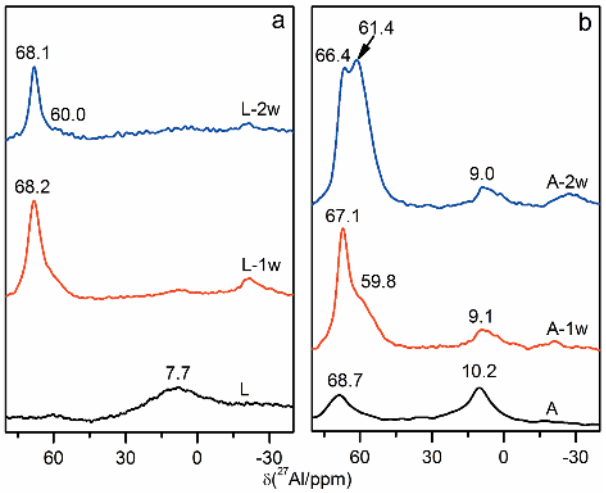

FIGURE 8. ^{27}Al MAS NMR spectra of serpentine and their hydrothermal products. (**a**) Lizardite and its hydrothermal products. The signal at 7.7 ppm disappears with the occurrence of the signal at approximately 68 ppm after hydrothermal treatment of lizardite. (**b**) Antigorite and its hydrothermal products. A new signal at approximately 60 ppm appears after hydrothermal treatment. The intensity of the signal at ca. 10 ppm decreases with the increase of those at approximately 69 and 60 ppm.

negative layer charge, which is compensated by exchangeable cations in the interlayer spaces. Subsequently, the basal spacing (d_{001}) of smectite is controlled by the nature of interlayer cations and their hydration state. For instance, Na-smectite with one-water layer in the interlayer space has a basal spacing of 1.2–1.3 nm (Ferrage et al. 2005). The occurrence of the reflections at 1.2–1.3 nm in the XRD patterns of the hydrothermal products (Fig. 1) is indicative of the formation of smectite (Sato et al. 1992; Ferrage et al. 2005). As $Na_2SiO_3 \cdot 9H_2O$ was used as one of the starting materials, the resultant smectite may have Na^+ as its interlayer cation. Meanwhile, TEM observations also provide convincible evidences for the successful transformation from serpentine to smectite. After hydrothermal treatment of lizardite and antigorite, the smectite layers with a thickness of approximately 1.3 nm can be extensively observed in the TEM images (Figs. 3–6) (Murakami et al. 1999; Kim et al. 2004; Bisio et al. 2008; He et al. 2017). And the Si/Mg ratios of these layers, determined by EDS analyses, are almost identical with that of smectite (Fig. 7).

Note that the changes of XRD patterns for lizardite and antigorite before and after hydrothermal treatment are dramatically different. For antigorite, the XRD patterns of hydrothermal products display prominent reflections of antigorite precursor, suggesting that most parts of antigorite remain unchanged. This is also supported by the HRTEM images in which the newly formed smectite is only observed at the edge of the antigorite particles rather than within them. However, in the case of lizardite, despite the weak reflection of smectite, the characteristic (001) reflection at 0.72 nm dramatically decreased after hydrothermal treatment. HRTEM observations indicate that the conversion of lizardite to smectite can occur in different domains within lizardite particles, accompanied by layer distortion and exfoliation. This may result in the dramatic decrease of characteristic reflection of lizardite and the occurrence of weak reflections of smectite (Lan and Pinnavaia 1994; Watkins and McCarthy 1995; Dennis et al. 2001). The occurrence of intense reflections of quartz [e.g., (101) and (100) reflections] in the XRD patterns of hydrothermal products and the increase of their intensity with an extension of reaction time strongly suggests that the added metasilicate did not completely react with serpentine minerals, and polymerization of metasilicate led to the formation of quartz.

Compared to the transformation of kaolinite and halloysite into smectite (He et al. 2017), the transformation of serpentine (e.g., lizardite and antigorite) into smectite is much more difficult. In our recent studies (He et al. 2014, 2017), the substitution of Al^{3+} for Si^{4+} in the tetrahedral sheets has been proved to be critical for improving the size matching between octahedral and tetrahedral sheets of smectite. EDS analyses of the hydrothermal products show that the Al/Mg ratios of the newly formed smectite are slightly higher than that of the corresponding serpentine minerals (Fig. 7). This suggests that Al atoms are incorporated into the neo-formed smectite during the transformation, which are provided by the dissolution of the octahedral sheets of the starting serpentine. Our ^{27}Al MAS NMR spectra further demonstrate that these Al atoms enter into the Si-O tetrahedral sheets via the substitution of Al^{3+} for Si^{4+}. Thus, the difficulty of the transformation from serpentine to smectite may be due to the low Al content in the starting serpentine minerals (Table 1), which is the available Al source for the substitution of Al^{3+} for Si^{4+}. Our calculation, based on the powder XRD patterns, shows that the ratios of the newly formed smectite in the hydrothermal products from antigorite (A-2w) and lizardite (L-2w) are 28.3 and 57.3% (Table 2), respectively. Such significant difference between the transformation ratios from antigorite and lizardite may be mainly controlled by their structure and the transformation mechanism involved as well as the low Al content in precursor minerals.

Transformation mechanism

The structural unit of serpentine has a polar layer with a thickness of 0.72 nm, which is composed of one tetrahedral sheet and one octahedral sheet (Wicks and Whittaker 1975; Mellini 1982; Grobéty 2003; Palacios-Lidon et al. 2010; Evans et al. 2013). Lizardite and antigorite have similar theoretical formula of $Mg_3Si_2O_5(OH)_4$ but with different extents and types of isomorphous substitution (e.g., lizardite is rich in Al and Fe, and antigorite is rich in Si) (Uehara and Shirozu 1985; O'Hanley and Dyar 1993). The linking ways of neighboring layers for serpentine minerals are very different from each other. The adjacent layers in lizardite are linked via hydrogen bonds. However, in antigorite, the octahedral sheet is continuous and wavy, whereas the tetrahedral sheet undergoes periodic reversals. Thus, antigorite layers are bound through strong covalent Si-O bonds connecting the reversals (Evans et al. 2013). For smectite, its unit layer consists of an octahedral sheet sandwiched between two opposing tetrahedral sheets (Kloprogge et al. 1999; Bisio et al. 2008). Due to isomorphous substitutions (e.g., Al^{3+} by Mg^{2+}, or Mg^{2+} by Li^+, in the octahedral sheet; and Si^{4+} by Al^{3+} in the tetrahedral sheet), the layers are negatively charged, which is balanced by exchangeable interlayer cation (Brigatti et al. 2013). According to the essential structural dif-

ference between serpentine and smectite, one Si-O tetrahedral sheet must be attached onto the octahedral sheet of serpentine if the transformation of serpentine to smectite takes place via solid-state mechanism.

As indicated by the HRTEM images (Fig. 3), two dominant transformation pathways take place in the conversion of lizardite to smectite. One is the conversion of lizardite layers to the same number of smectite layers (Figs. 3d–3f) through the reaction of TO (lizardite layer) + T → TOT (smectite layer) (Fig. 9a). The extra tetrahedral sheets (T) are formed through attachment Si-O tetrahedra (i.e., hydrolyzed metasilicate in reaction solution) onto the octahedral sheets of the lizardite layers, which is followed by condensation between inner-surface hydroxyls and hydrolyzed metasilicate (He et al. 2017). This suggests a solid-state mechanism involved in the transformation (Amouric and Olives 1998; He et al. 2017). Thus, the thickness of the neo-formed layers increases to 1.3 nm from 0.7 nm in lizardite, in which the expansion of the newly formed smectite layer results in squeezing the interlayer space between the smectite layer and its adjacent lizardite layer (Figs. 3d and 3e). This will lead to distortion and exfoliation of phyllosilicate layers in the hydrothermal products and significant decrease of particles size and layer number contained therein (Fig. 9a), consistent with the weak (001) reflections of the hydrothermal products (Fig. 1a). Such transformation procedure is similar to that from kaolinite to beidellite as our previous report (He et al. 2017).

The other pathway is merging of two lizardite layers into one smectite layer through a reaction of 2TO → TOT + Mg^{2+}/Al^{3+}, which is accompanied with dissolution of octahedral sheets and inversion of one tetrahedral sheet in one lizardite layer (Fig. 9a). Such conversion via partial dissolution of the initial serpentine structure (i.e., octahedral sheet) with recombination of Si-O sheet and serpentine layer to form smectite layers can also be regarded as solid-state transformation (Altaner and Ylagan 1997; Amouric and Olives 1998; Banfield and Murakami 1998; Cuadros and Altaner 1998; Lindgreen et al. 2000; Dudek et al. 2006; Cuardos 2012). As shown by HRTEM images (Fig. 3c), 15 lizardite layers (TO) are observed at the central area of Sampler L-2w (left red rectangle in Fig. 3c), while only 8 smectite layers (TOT) occur at the edge of this particle (right red rectangle in Fig. 3c). This strongly suggests that dissolution of Mg-octahedral sheets took place during the transformation. However, our measurements show that the concentration of Mg in the supernatant solution is lower than 1 ppm. This seems to be contradictory with the proposal about the dissolution of Mg-octahedral sheets. Our HRTEM observation shows that a small amount of pure smectite particles, without any lizardite layers, occurs in the hydrothermal products (Fig. 4). As no additional Mg source was added into the reaction system, in which lizardite is the only phase containing Mg. Hence, these pure smectite particles should be formed by the reaction between the dissolved Mg

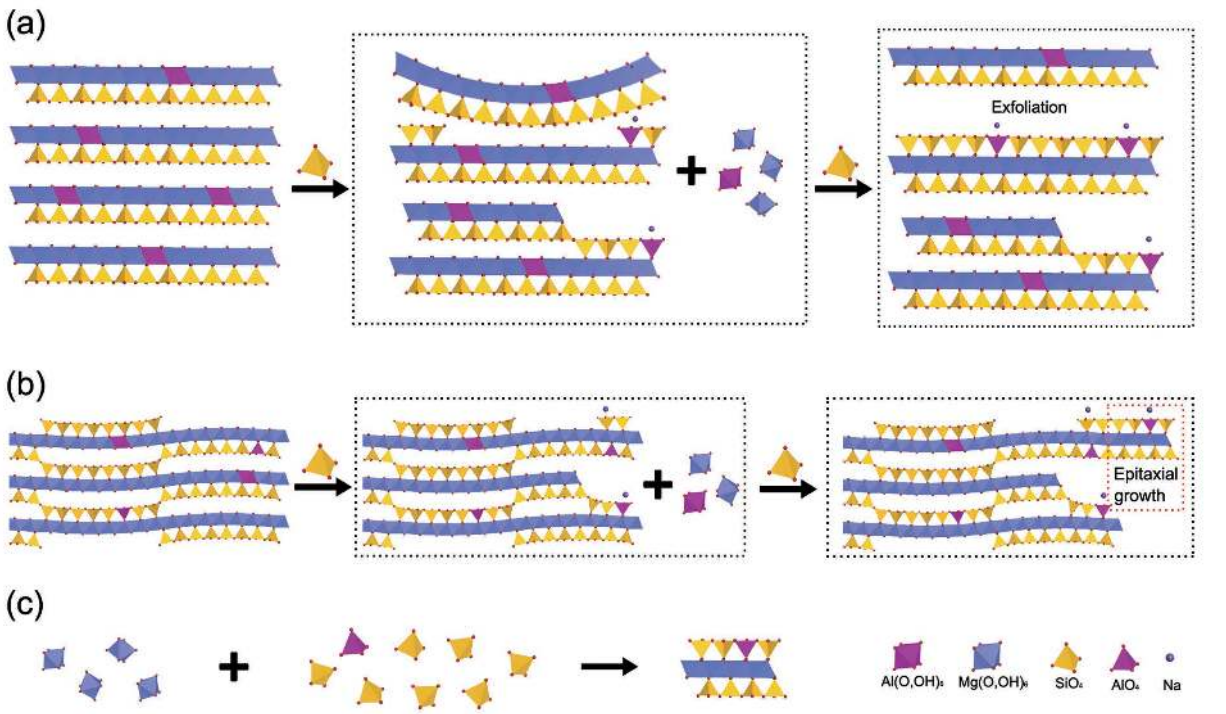

FIGURE 9. The schematic diagram for the transformation processes of lizardite and antigorite. (**a**) Two solid-state transformation pathways in lizardite: transformation from one serpentine layer into one smectite layer, accompanied with exfoliation (upper) and merging of two serpentine layers into one smectite layer (down). (**b**) Epitaxial growth and two solid-state transformation pathways in antigorite. Epitaxial growth occurs at the edge of the newly formed smectite layers around antigorite particles. (**c**) The dissolution-reprecipitation transformation pathway involved in the transformation from lizardite to smectite, which is not as important as the solid-state transformation ones involved. The Mg and Al sources were supplied during the process displayed in **a**.

and metasilicate, resulting in a very low Mg concentration in the solution. This reflects that a dissolution-reprecipatation mechanism is also involved in the transformation, but not as dominant as solid-state transformation.

In comparison to lizardite, the transformation of antigorite into smectite is much more difficult. Our calculation, based on the powder XRD patterns, shows that only 28.3% of antigorite was successfully converted to smectite. The calculated result is well coincident with the HRTEM observations of the hydrothermal products, in which the newly formed smectite layers were only formed along the edges of the starting antigorite particles and no smectite layers were observed within the antigorite domains (Fig. 5b). This is very different from the transformation of lizardite as discussed above. The occurrence of such transformation is due to the unique structure of antigorite. For the supercells in the inner part of antigorite layer, both the ends are fixed by the strong Si-O covalent bonds between the two adjacent layers (Evans et al. 2013), hindering the transformation from antigorite to smectite. However, for the supercell at the edge of a certain layer, the end toward inner side is fixed by the covalent Si-O bond whereas the other end toward outside does not have such fixation, similar to the lizardite layer to some extent. Accordingly, both the two transformation pathways, conversion of one antigorite layer to one smectite layer and two adjacent antigorite layers merging into one smectite layer, occur at the edge of antigorite particles (Figs. 5c and 9b), corresponding to a solid-state mechanism (Banfield and Bailey 1996; Xu and Veblen 1996; Amouric and Olives 1998; He et al. 2017). As indicated by the HRTEM images (Fig. 5c), newly formed smectite layers are well connected with the antigorite layers, and the length of the neo-formed smectite layers is longer (most located at the range of 5–10 nm, Figs. 5 and 6) than that of a half the supercell repeat-unit in antigorite (approximately 1.6 nm). This reflects that epitaxial growth of smectite layers is also involved in the transformation, which could be regarded as a dissolution-reprecipatation procedure. As antigorite is the only phase containing Mg and no additional Mg source was added in this reaction system, the released Mg, due to the dissolution of octahedral sheet, is the main Mg source for epitaxial growth of smectite layers (Starcher et al. 2017).

To exclude the potential effects of the starting mineral dissolution on their transformation, dissolution experiments were conducted under the identical conditions but without adding any sodium metasilicate. No reflections at approximately 1.3 nm, corresponding to the basal spacing of smectite, were recorded in the XRD patterns of the hydrothermal products (not show). This is consistent with their HRTEM images (not show) in which no smectite layers and distortion of serpentine layers were observed. Meanwhile, our measurements showed that the Mg concentration in the supernatant solution is as low as 2–3 ppm. These investigations suggest that no significant dissolution of the starting serpentine minerals took place under the identical *P-T* condition (without adding Si source). In other words, an existence of additional Si source is essential for the transformation of serpentine into smectite. This is in agreement with the insights deduced from the conversion of halloysite and kaolinite to beidellite (He et al. 2017).

Implication

Our present study demonstrates that 1:1 type serpentine minerals (i.e., lizardite and antigorite) can be transformed into 2:1 type smectite under hydrothermal condition. In this procedure, one serpentine layer can be converted to one smectite layer via attachment of Si-O tetrahedra onto the octahedral sheet surface of the starting minerals, and two adjacent serpentine layers can be merged into one smectite layer (Fig. 9). In the latter case, dissolution of Mg-octahedral sheets and inversion of tetrahedral sheets take place. Both the two pathways suggest that the solid-state mechanism is involved in the transformation of serpentine minerals into smectite (Banfield and Bailey 1996; Xu and Veblen 1996; Amouric and Olives 1998; He et al. 2017). Due to the dissolution of Mg-octahedral sheets, free Mg cations are released into the reaction system and they can react with metasilicate to form smectite. Certainly, a small amount of Al cations are simultaneously released in this procedure and most of them are incorporated into the newly formed Si-O tetrahedral sheets of smectite, as indicated by ^{27}Al MAS NMR spectra. Such substitution of Al^{3+} for Si^{4+}, which can improve the size matching between octahedral and tetrahedral sheets of smectite, has important effect on a successful transformation and conversion rate from serpentine to smectite. However, in comparison to the transformation of kaolinite group minerals to beidelite under identical experimental conditions, the transformation of serpentine minerals is more complex. Besides the solid-state transformation ways, epitaxial growth of smectite occurred in the conversion of antigorite while precipitation happened in the case of lizardite. This suggests that the microstructure of the starting minerals have important effects on their transformation procedures and crystallochemical characteristics of the resulting minerals. This insight would be helpful for better understanding phyllosilicate crystal chemistry. For example, due to the adjacent antigorite layers linked by the strong Si-O covalent bonds, the epitaxial growth of smectite was observed in the transformation. Similarly, the neighboring layers in mica group minerals are linked via strong electrostatic force, and they always display large particle size. This implies that a strong physicochemical interaction (as well as similarity in chemical compositions) between the adjacent layers in phyllosilicates (Charlet and Manceau 1994; Ji et al. 2013; Yang et al. 2015; Starcher et al. 2017) is critical for epitaxial growth. Maybe, this can well explain the interesting phenomenon that mica group minerals always display large crystal size, whereas the size of smectite group minerals are less than several micrometers.

On the other hand, serpentine minerals are an important component of the oceanic crust, and they play a chief role in lithosphere dynamics (Viti 2010). Our present experimental study demonstrates that the transformation of serpentine into smectite is feasible, especially for lizardite, under hydrothermal environment with the presence of SiO_2, but without any evidence for the formation of talc. However, voluminous literature reported that serpentine could be converted to talc in SiO_2-rich fluid systems without occurrence of smectite. Due to chemical and structural variations, talc and smectite have significant differences in water content, cation mobility, and physicochemical properties. Thus, they can exert great influences on rock volume, rock rheology, and rock permeability, with subsequent effects

on subduction zones, fault dynamics, and seismic behavior (Moore and Saffer 2001; Peacock 2001; Moore and Rymer 2007; Lockner et al. 2011). Our present study implies the possibility for the conversion of serpentine to smectite in nature. Hence, detailed mineralogical identification of hydrothermal products of serpentine in various natural systems, as well as comprehensive investigations on the geochemical conditions for occurrence of talc and/or smectite transformed from precursor serpentine, are needed in further study.

Acknowledgments

This is contribution No. IS-2473 from GIGCAS. This work was financially supported by National Natural Science Foundation of China (Grant Nos. 41530313), CAS Key Research Program of Frontier Sciences (Grant No. QYZDJ-SSW-DQC023), the CAS/SAFEA International Partnership Program for Creative Research Teams (Grant No. 20140491534) and Natural Science Foundation of Guangdong Province, China (Grant No. S201303001424). The authors thank Warren Huff for handling this paper, and Alain Decarreau and Huifang Xu for reviewing the manuscript and providing constructive comments.

References cited

Altaner, S.P., and Ylagan, R.F. (1997) Comparison of structural models of mixed-layer illite/smectite and reaction mechanisms of smectite illitization. Clays and Clay Minerals, 45, 517–533.

Altschuler, Z.S., Dwornik, E.J., and Kramer, H. (1963) Transformation of montmorillonite to kaolinite during weathering. Science, 141, 148–152.

Amouric, M., and Olives, J. (1998) Transformaion mechanisms and interstratification in converstion of smectite to kaolinite: An HRTEM study. Clays and Clay Minerals, 46, 521–527.

Banfield, J.F., and Bailey, S.W. (1996) Formation of regularly interstratified serpentine-chlorite minerals by tetrahedral inversion in long-period serpentine polytypes. American Mineralogist, 81, 79–91.

Banfield, J.F., and Murakami, T. (1998) Atomic-resolution transmission electron microscope evidence for the mechanism by which chlorite weathers to 1:1 semi-regular chlorite-vermiculite. American Mineralogist, 83, 348–357.

Beaufort, D., Rigault, C., Billon, S., Billault, V., Inoue, A., Inoue, S., and Patrier, P. (2015) Chlorite and chloritization processes through mixed-layer mineral series in low-temperature geological systems - a review. Clay Minerals, 50, 497–523.

Bentabol, M., Cruz, R., and Sobrados, I. (2010) Chemistry, morphology and structural characteristics of synthethc Al-lizardite. Clay Minerals, 45, 131–143.

Bergaya, F., and Lagaly, G. (2013) General introduction: Clays, clay minerals, and clay science. In F. Bergaya and G. Lagaly, Eds., Handbook of Clay Science, p. 16. Elsevier.

Bisio, C., Gatti, G., Boccaleri, E., Marchese, L., Superti, G.B., Pastore, H.O., and Thommes, M. (2008) Understanding physico–chemical properties of saponite synthetic clays. Microporous and Mesoporous Materials, 107, 90–101.

Boles, J.R., and Franks, S.G. (1979) Clay diagenesis in Wilcox sandstones of southwest Texas: Implications of smectite diagenesis on sandstone cementation. Journal of Sedimentary Petrology, 49, 55–70.

Bonifacio, E., Zanini, E., Boero, V., and Franchini-Angela, M. (1997) Pedogenesis in a soil catena on serpentinite in north-western Italy. Geoderma, 75, 33–51.

Breen, C., Madejová, J., and Komadel, P. (1995) Correlation of catalytic activity with infra-red, ^{29}Si MAS NMR and acidity data for HCl-treated fine fractions of montmorillonites. Applied Clay Science, 10, 219–230.

Brigatti, M.F., Galán, E., and Theng, B.K.G. (2013) Structure and mineralogy of clay minerals. In F. Bergaya and G. Lagaly, Eds., Handbook of Clay Science, p. 42–45. Elsevier.

Brindley, G.W. (1980a) Order-disorder in clay mineral structures. In G.W. Brindley and G. Brown, Eds., Crystal Structure of Clay Minerals and Their X-ray Identification, p. 125–196. Mineralogical Society, London.

——— (1980b) Quantitative X-ray mineral analysis of clays. In G.W. Brindley and G. Brown, Eds., Crystal Structure of Clay Minerals and Their X-ray Identification, p. 411–438. Mineralogical Society, London.

Capitani, G., and Mellini, M. (2004) The modulated crystal structure of antigorite: The m = 17 polysome. American Mineralogist, 89, 147–158.

Chang, C.P., Angelier, J., and Huang, C.P. (2000) Origin and evolution of a mélange: the active plate boundary and suture zone of the Longitudiual Valley, Taiwan. Tectonophysics, 325, 43–62.

Charlet, L., and Manceau, A. (1994) Evidence for the neoformation of clays upon sorption of Co(II) and Ni(II) on silicates. Geochimica et Cosmochimica Acta, 58, 2577–2582.

Coombe, D.E., Frost, L.C., Le Bas, M., and Watters, W. (1956) The nature and origin of the soils over the Cornish serpentine. Journal of Ecology, 44, 605–615.

Cuadros, J. (2012) Clay crystal-chemical adaptability and transformation mechanisms. Clay Minerals, 47, 147–164.

Cuadros, J., and Altaner, S.P. (1998) Characterization of mixed-layer illite-smectite from bentonites using microscopic, chemical, and X-ray methods: Constraints on the smectite-to-illite transformation mechanism. American Mineralogist, 83, 762–774.

Dennis, H.R., Hunter, D.L., Chang, D., Kim, S., White, J.L., Cho, J.W., and Paul, D.R. (2001) Effect of melt processing conditions on the extent of exfoliation in organoclay-based nanocomposites. Polymer, 42, 9513–9522.

Ducloux, J., Meunier, A., and Velde, B. (1976) Smectite, chlorite, and a regular interlayered chlorite-vermiculite in soils developed on a small serpentinite body, Massif Central, France. Clay Minerals, 11, 121–135.

Dudek, T., Cuadros, J., and Fiore, S. (2006) Interstratified kaolinite-smectite: Nature of the layers and mechanism of smectite kaolinization. American Mineralogist, 91, 159–170.

Dunoyer de Segonzac, G. (1970) The transformation of clay minerals during diagenesis and low-grade metamorphism: A review. Sedimentology, 15, 281–346.

Evans, B.W., Hattori, K., and Baronnet, A. (2013) Serpentinite: what, why, where? Elements, 9, 99–106.

Ferrage, E., Lanson, B., Malikova, N., Plançon, A., Sakharov, B.A., and Drits, V.A. (2005) New insights on the distribution of interlayer water in bi-hydrated smectite from X-ray diffraction profile modeling of 00*l* reflections. Chemistry of Materials, 17, 3499–3512.

Ferrage, E., Lanson, B., Michot, L.J., and Robert, J.-L. (2010) Hydration properties and interlayer organization of water and ions in synthetic Na-smectite with tetrahedral layer charge. Part 1. Results from X-ray diffraction profile modeling. The Journal of Physical Chemistry C, 114, 4515–4526.

Graham, R.C., Diallo, M.M., and Lund, L.J. (1990) Soils and mineral weathering on phyllite colluvium and serpentinite in northwestern California. Soil Science Society of America Journal, 54, 1682–1690.

Grobéty, B. (2003) Polytypes and higher-order structures of antigorite: A TEM study. American Mineralogist, 88, 27–36.

He, H.P., Li, T., Tao, Q., Chen, T.H., Zhang, D., Zhu, J.X., Yuan, P., and Zhu, R.L. (2014) Aluminum ion occupancy in the structure of synthetic saponites: Effect on crystallinity. American Mineralogist, 99, 109–116.

He, H.P., Ji, S.C., Tao, Q., Zhu, J.X., Chen, T.H., Liang, X.L., Li, Z.H., and Dong, H.L. (2017) Transformation of halloysite and kaolinite into beidellite under hydrothermal condition. American Mineralogist, 102, 997–1005.

Hower, J., Eslinger, E.V., Hower, M.E., and Perry, E.A. (1976) Mechnism of burial metamorphism of argillaceous sediment: 1. Mineralogical and chemical evidence. Geological Society of America Bulletin, 87, 725–737.

Istok, J.D., and Harward, M.E. (1982) Influence of soil moisture on smectite formation in soils derived from serpentinite. Soil Science Society of America Journal, 46, 1106–1108.

Ji, Q., Zhang, Y.F., Gao, T., Zhang, Y., Ma, D.L., Liu, M.X., Chen, Y.B., Qiao, X.F., Tan, P.H., Kan, M., Feng, J., Sun, Q., and Liu, Z.F. (2013) Epitaxial monolayer MoS_2 on mica with novel photoluminescence. Nano Letters, 13, 3870–3877.

Kim, J., Dong, H., Seabaugh, J., Newell, S.W., and Ebert, D.D. (2004) Role of microbes in the smectite-to-illite reaction. Science, 303, 830–832.

Kloprogge, J.T., Komarneni, S., and Amonette, J.E. (1999) Synthesis of smectite clay minerals: A critical review. Clays and Clay Minerals, 47, 529–554.

Kunze, G. (1956) Die gewellte Struktur des Antigorits, I. Zeitschrift für Kristallograhie, 108, 82–107.

——— (1958) Die gewellte Struktur des Antigorits, II. Zeitschrift für Kristallograhie, 110, 282–320.

——— (1961) Antigorit. Strukturtheoretische Grundlagen und ihre praktische Bedeutung für die weitere Serpentin-Forschung. Fortschritte der Mineralogie, 39, 206–324.

Lan, T., and Pinnavaia, T.J. (1994) Clay-reinforced epoxy nanocomposites. Chemistry of Materials, 6, 2216–2219.

Lanson, B., Beaufort, D., Berger, G., Baradat, J., and Lacharpagen, J.C. (1996) Illitization of diagenetic kaolinite-to-dickite conversion series: Late-stage diagenesis of the Lower Permian Potliegend sandstone reservoir, offshore of the Netherlands. Journal of Sedimentary Research, 66, 501–518.

Lee, B.D., Sears, S.K., Graham, R.C., Amrhein, C., and Vali, H. (2003) Secondary mineral genesis from chlorite and serpentine in an ultramafic soil toposequence. Soil Science Society of America Journal, 67, 1309–1317.

Lindgreen, H., Drits, V.A., Sakharov, B.A., Salyn, A.L., Wrang, P., and Dainyak, L.G. (2000) Illite-smectite structural changes during metamorphism in black Cambrian Alum shales from the Baltic area. American Mineralogist, 85, 1223–1238.

Lockner, D.A., Morrow, C., Moore, D., and Hickman, S. (2011) Low strength of deep San Andreas fault gouge from SAFOD core. Nature, 472, 82–85.

Mackumbi, L., and Herbillon, A.J. (1972) Vermiculitisation expérimentale d'une chlorite. Bulletin de Groups Français des Argiles, 24, 153–164.

Mellini, M. (1982) The crystal structure of lizardite 1*T*: hydrogen bonds and polytypism. American Mineralogist, 67, 587–598.

Moore, D.E., and Rymer, M.J. (2007) Talc-bearing serpentinite and the crweeping section of the San Andreas fault. Nature, 448, 795–797.

Moore, J.C., and Saffer, D. (2001) Updip limit of the seismogenic zone beneath the

accretionary prism of southwest Japan: An effect of diagenetic to low-grade metamorphic processes and increasing effective stress. Geology, 29, 183–186.
Mosser-Ruck, R., Devineau, K., Charpentier, D., and Cathelineau, M. (2005) Effects of ethylene glycol saturation protocols on XRD patterns: A critical review and discussion. Clays and Clay Minerals, 53, 631–638.
Murakami, T., Sato, T., and Inoue, A. (1999) HRTEM evidence for the process and mechanism of saponite-to-chlorite conversion through corrensite. American Mineralogist, 84, 1080–1087.
Nadeau, P.H., Wilson, M.J., McHardy, W.J., and Tait, J.M. (1985) The conversion of smectite to illite during diagenesis: evidence from some illitic clays from bentonites and sandstones. Mineralogical Magazine, 49, 393–400.
Odin, G.S. (1988) Glaucony from the Gulf of Guinea. In G.S. Odin, Ed., Green Marine Clays: Oolitic Ironstone Facies, Verdine Facies, Glaucony Facies and Celadonite-Bearing Facies—A Comparative Study, p. 225–248. Elsevier, Amsterdam.
O'Hanley, D.S., and Dyar, M.D. (1993) The composition of lizardite 1*T* and the formation of magnetite in serpentinites. American Mineralogist, 78, 391–404.
Otten, M.T. (1993) High-resolution transmission electron microscopy of polysomatism and stacking defects in antigorite. American Mineralogist, 78, 75–84.
Palacios-Lidon, E., Grauby, O., Henry, C., Astier, J.-P., Barth, C., and Baronnet, A. (2010) TEM-assisted dynamic scanning force microscope imaging of (001) ntigorite: Surfaces and steps on a modulated silicate. American Mineralogist, 95, 673–685.
Peacock, S.M. (2001) Are the lower planes of double seismic zones caused by serpentine dehydration in subducting oceanic mantle? Geology, 29, 299–302.
Pollard, C.O. (1971) Appendix: Semi-displacive mechanism for diagenetic alteration of montmorillonite layers to illite layers. Geological Society of America, Special Paper, 134, 79–93.
Righi, D., Terribile, F., and Petit, S. (1999) Pedogenic formation of kaolinite-smectite mixed layers in a soil toposequence developed from basaltic parent material in Sardinia (Italy). Clays and Clay Minerals, 47, 505–514.
Ryan, P.C., and Huertas, F.J. (2013) Reaction pathways of clay minerals in tropical soils: Insights from kaolinite-smectite synthesis experiments. Clays and Clay Minerals, 61, 303–318.
Ryan, P.C., and Reynolds, R.C. Jr. (1997) The chemical composition of serpentine/chlorite in the Tuscaloosa formation, United States Gulf coast: EDX vs. XRD determinations, implications for mineralogic reactions and the origin of anatase. Clays and Clay Minerals, 45, 339–352.
Ryu, K.W., Jang, Y.N., Chae, O.C., Bae, I.K., and Choi, S.H. (2006) Hydrothermal synthesis of smectite from dickite. Clays and Clay Minerals, 54, 80–86.
Sato, T., Watanabe, T., and Otsuka, R. (1992) Effects of layer charge, charge location, and energy change on expansion properities of dioctahedral smectites. Clays and Clay Minerals, 40, 103–113.
Schumann, D., Hartman, H., Eberl, D.D., Sears, S.K., Hesse, R., and Vali, H. (2013) The influence of oxalate-promoted growth of saponite and talc crystals on rectorite: Testing the intercalation-synthesis hypothesis of 2:1 layer silicates. Clays and Clay Minerals, 61, 342–360.
Starcher, A.N., Elzinga, E.J., and Sparks, D.L. (2017) Formation of a mixed Fe(II)-Zn-Al layered hydroxide: Effects of Zn co-sorption on Fe(II) layered hydroxide formation and kinetics. Chemical Geology, 464, 46–56.
Stripp, G.R., Field, M., Schumacher, J.C., Sparks, R.S.J., and Cressey, G. (2006) Post-emplacement serpentinization and related hydrothermal metamorphism in a kimberlite from Venetica, South Africa. Journal of Metamorphic Geology, 24, 515–534.
Suquet, H., de le Calle, C., and Pezerat, H. (1975) Swelling and structural organization of saponite. Clays and Clay Minerals, 23, 1–9.
Uehara, S. (1988) TEM and XRD study of antigorite superstructures. Canadian Mineralogist, 36, 1595–1605.
Uehara, S., and Shirozu, H. (1985) Variations in chemical composition and structural properties of antigorites. Mineralogical Journal, 12, 299–318.
Viti, C. (2010) Serpentine minerals discrimination by thermal analysis. American Mineralogist, 95, 631–638.
Watkins, J.J., and McCarthy, T.J. (1995) Polymer/metal nanocomposite synthesis in supercritical CO_2. Chemistry of Materials, 7, 1991–1994.
Weaver, C.E. (1958) The effects and geological significance of potassium "fixation" by expandable clay minerals derived from muscovite, biotite, chlorite, and volcanic material. American Mineralogist, 43, 839–861.
Wicks, F.J., and Whittaker, E.J.W. (1975) A reappraisal of the structures of the serpentine minerals. Canadian Mineralogist, 13, 227–243.
Wildman, W.E., Jackson, M.L., and Whittig, L.D. (1968) Iron-rich montmorillonite formation in soils derived from serpentine. Soil Science Society of America Journal, 32, 787–794.
Wilson, M.J. (2004) Weathering of the primary rock-forming minerals: processes, products and rates. Clay Minerals, 39, 233–266.
Whittaker, E.J.W., and Zussman, J. (1956) The characterization of serpentine minerals by X-ray diffraction. Mineralogical Magazine, 31, 107–126.
Woessner, D.E. (1989) Characterization of clay minerals by ^{27}Al nuclear magnetic resonance spectroscopy. American Mineralogist, 74, 203–215.
Wooster, N., and Wooster, W.A. (1946) Preparation of synthetic quartz. Nature, 157, 297.
Xu, H.F., and Veblen, D.R. (1996) Interstratification and other reaction microstructures in the chlorite–berthierine series. Contributions to Mineralogy and Petrology, 124, 291–301.
Yang, S.T., Ren, X.M., Zhao, G.X., Shi, W.Q., Montavon, G., Grambow, B., and Wang, X.K. (2015) Competitive sorption and selective sequence of Cu(II) and Ni(II) on montmorillonite: Batch, modeling, EPR and XAS studied. Geochimica et Cosmochimica Acta, 166, 129–145.
Zussman, J. (1954) Investigation of the crystal structure of antigorite. Mineralogical Magazine, 30, 498–512.

Manuscript received May 8, 2017
Manuscript accepted October 30, 2017
Manuscript handled by Warren D. Huff